Improved geophysical monitoring of carbon sequestration through parameter linkage to reservoir modeling.

Authors: Michael Commer, Erika Gasperikova, Christine Doughty

Earth and Environmental Sciences Area, Lawrence Berkeley National Laboratory, Berkeley, CA, United States

ABSTRACT

Predictive reservoir modeling, even if present in the form of only basic hydrogeological model assumptions, is expected to accompany the majority of carbon capture and sequestration monitoring activities. It thus represents a source of prior information about the migration of injected fluids that can benefit geophysical survey planning and ensuing monitoring. Constraining the imaging of geophysical monitoring data with reservoir modeling is preferable over standalone geophysical imaging because of additional complementary hydrogeological information. However, fully coupled hydrogeophysical data inversion for flow-modeling parameters that control saturation predictions is an involved process. Within the context of three-dimensional electromagnetic (EM) inversion of data from borehole-to-surface layouts, we employ a "poor people's" alternative. The approach constrains geophysical inversion parameters through saturation predictions. The coupling is realized through spatially variable lower and upper parameter bounds that scale with gas saturation magnitudes, the latter provided by reservoir modeling. Enhancement of three-dimensional time-lapse plume EM imaging is demonstrated for simulated sequestration into a depleted gas reservoir.

1. Introduction

Regional-scale deployment of geologic carbon sequestration (GCS) requires reliable stewardship in form of failsafe monitoring in order to reach industrial maturity (e.g., Arts et al., 2008; Shi et al., 2008; Ringrose, 2020). Geophysical remote-sensing methods offer the volume coverage needed for long-term monitoring of regional-scale GCS activities (Gasperikova and Hoversten, 2006; Michael et al., 2010; Jenkins et al., 2015; Davis et al., 2019; Gasperikova et al., 2022; Tveit and Mannseth, 2022). Among geophysical rock properties, electrical properties have shown to correlate with saturation levels of stored carbon dioxide (CO_2) in a porous system (Kim et al., 2010; Alemu et al., 2011). Owing to their sensitivity to fluid-induced electrical property changes and large exploration depths, geophysical controlled-source electromagnetic (CSEM) methods (e.g., Streich et al., 2010; Wirianto et al., 2010; Vilamajó et al., 2013) and concomitant CSEM-data inversion methods (e.g., Ayani et al., 2020; Grana et al., 2021; Tveit et al., 2015; Tveit et al., 2020) have become viable techniques for GCS monitoring.

Typical reservoir depths exceed 800 m in order to meet the pressure and temperature requirements needed to store CO_2 as a supercritical fluid (van der Meer, 1993). Large reservoir depths render borehole-to-surface electromagnetic (BSEM) surveying as suitable because the proximity of transmitters to target zones retains its sensitivities (He et al., 2005; Marsala et al., 2011; Gasperikova et al., 2022). BSEM is defined by a borehole-deployed transmitter and a receiver spread on the surface. Despite its advantage of strategically placing instruments near zones of interest, a major challenge to deep reservoir monitoring is a typically thin nature of fluid-confining formations (Marsala et al., 2014). There is growing consensus that vertical electric dipole (VED) antennas deployed as sources can alleviate this issue because their dominating EM-wave mode maximizes sensitivities to thin target structures (Wirianto et al., 2010; Girard et al., 2011; Vilamajó et al., 2013; Grayver et al., 2014; Schaller et al., 2014).

While technical feasibility can be regarded as established, we believe that economic feasibility is an equally important but more overlooked aspect. This contribution simulates a low-cost scenario by making the BSEM survey design deliberately sparse in terms of the total instrumentation. While we exploit the resolution advantages of VED sources, the BSEM setup of our imaging demonstrations implies a volume coverage that is relatively small compared to the regional target scale. To offset the deficiencies due to a limited instrumentation, we propose the incorporation of model constraints provided by reservoir modeling.

Reservoir modeling (e.g., Hosseini et al., 2012) can be regarded as some subsurface equivalent to weather prediction because fluid flow and transport forecasting improves as more monitoring data becomes available over time. Reservoir models are expected to be a standard part of GCS site management. Doughty and Oldenburg (2020) use the term *operational* reservoir model for a hydrogeologic model that is expected to be initially crude at the pre-injection stage due to a limited data base. Operational reservoir modeling then involves the assimilation of the monitoring data stream for an ongoing model improvement. A model that is deemed sufficiently mature thus provides a free source of prior complementary information to help optimize geophysical plume-mapping. To offset weak model resolution due to limited instrumentation, we hence propose to employ flow predictions in order to construct inversion constraints in the form of target-adapted model parameter bounds.

Spatially variable (lower and upper) model parameter bounds facilitate the incorporation of prior information as inversion constraints (e.g., Abubakar et al., 2008; Sosa et al., 2013; Aghamiry et al., 2019; Ogarko et al., 2021), because parameter ranges can be scaled with uncertainties. Recent studies (Commer et al., 2022) in a crosswell EM context have employed spatially variable scaling of bound widths under a different premise. For poorly resolved interwell regions, it was shown that bound intervals that are enlarged with respect to a global default can benefit the solution-finding process. Principally, this is achieved through diminishing the chance for a premature convergence towards local solution minima. The approach is related to the concept of inversion constraints with a spatially varying degree of enforcement in order to balance out varying sensitivities inherent in a given survey geometry (Yi et al., 2003). In a similar manner, to locally enhance model fidelity, we augment lower and upper parameter bounds in zones where operational reservoir modeling predicts significant gas saturation changes.

For brevity, we will use the abbreviation ORM for operational reservoir model in the following. Section 2 outlines the hydrogeophysical aspects underlying the construction of spatially variable parameter bounds from an ORM. These bounds are the input to the constrained inversion of synthetic BSEM data simulated for a large-scale reservoir model. The inversion approach presented in Section 3 and results in Section 4 demonstrate that expanded parameter bounds have the potential to offset weak model resolution in thin target zones that undergo CO_2-induced changes in electrical conductivity.

2. Hydrogeophysical reservoir modeling

Our EM-imaging experiments are based on a reservoir model that is representative of typical large-scale depleted natural gas reservoirs in the Sacramento River Delta region of California. Reservoirs of this kind are prospective candidates for long-term storage. Extensive CO_2 plume evolution simulations by Doughty and Oldenburg (2020) assessed long-term forecasting uncertainties associated with pressure and saturation evolution. Their simulated scenario involves 8 Mt/year of CO_2 injection over 20 years.

Doughty and Oldenburg (2020) used two types of reservoir flow models: actual and operational (Fig. 1). The actual model (Fig. 1a) features a complex heterogeneous 3D permeability representation of a regional-scale geologic model of a depleted gas field. Stochastic modeling added small-scale spatial model heterogeneity to ensure a more realistic geological complexity. A high-permeability sandstone layer located between depths of 1.4 and 1.8 km forms the actual storage reservoir, its thickness averaging roughly 400 m. The storage reservoir is overlain by a very low permeability shale (not shown in Fig. 1) that serves as cap rock for the reservoir.

Starting from an initially crude vertically-layered representation, a series of progressively more complex reservoir models was derived. Their complexity reflected incorporation of the gradually increasing informational content due to the accumulation and history-matching of periodically sampled pressure, saturation, and gas composition data, simulated for a set of 14 observation wells. These wells are distributed over approximately 7×13 km^2 as indicated by black circles in the horizontal sections of Fig. 1. Fig. 1b shows the estimated permeability model that would be realistically available to the site operator after 5 years of injection and history-matching of the corresponding monitoring data.

The actual model represents the (unknown) true state. Synthetic-data generation is based on this model. The ORM represents the best available approximation to the true state at the time 5 years after start of injection (at time zero). Geophysical inversion constraints will be constructed from this model.

2.1. Geophysical monitoring objective: time-lapse gas saturation changes

Our monitoring objective employs the 5-year ORM (Fig. 1b) for making gas-saturation predictions for up to 12 years. Note that the 5-year timeframe refers to model maturity. In a real-world case, this maturity would be attained by history-matching the monitoring data collected up to 5 years. Predicting the reservoir state up to 12 years hence translates to matching the 5-year monitoring history and forecasting the 7 following years. Fig. 2 (left column) compares the 12-year forecast of gas saturations between the actual model (a) and (b) the ORM. Striking is the more heterogeneous distribution of zones of altered gas saturations at 12 years in the actual model (compare subplots of left plot column). While the match is poor on a fine-scale, the ORM appears to reproduce regions of heightened saturations on a gross scale.

Gas saturation includes CH_4 (methane) and CO_2. Isolated pockets of gas as visible in Fig. 2a (left) have different origins. First, residual free-phase CH_4 is initially trapped in some attic regions forming static accumulations. Second, over the course of injection, degassed CH_4 can form due to addition of CO_2. Third, injection-induced changes in pressure and composition can create isolated free-phase CO_2 out of dissolved CO_2 as the latter is present more widely.

Our inversion objective is based on earlier assessments about the storage potential of the Sacramento River Delta region (Oldenburg et al., 2001). The region hosts many geological structures with gas storage capacity. Reinjecting gas into a depleted reservoir associates the question of permanence with properly forecasting where buoyant rise would make the gas accumulate over time. Therefore, we choose the attic region underneath the caprock (indicated as Northern attic in Fig. 1 and Fig. 2) as focus area as it is representative for locally closed high-permeability structures that are crucial as long-term repositories. To predict saturation changes due to fluid transfer and substitution processes, we choose the time span between 8 and 12 years. Fig. 2a (right column) exhibits that the particular permeability makeup of the actual model leads to significant saturation changes within this time interval. Properly forecasting these changes in the reservoir cap region can aid the reduction of reservoir performance uncertainty.

The ORM's prediction of the time-lapse saturation change between 8 and 12 years (Fig. 2b, right column) appears similar to the absolute saturations: there exists agreement on a gross scale; however, saturation changes in the Northern attic region appear with an error in the predicted elevation. Our objective thus also involves the question to what degree deviations from the true case would corrupt geophysical-data inversions that use prior information derived from the ORM.

2.2. Petrophysical transformation of the reservoir model

Petrophysical transformation functions are the key linking elements between two physical systems: the reservoir flow model and the geophysical model for EM data simulation. The petrophysical relationship derived in the following establishes a connection between rock properties that control fluid transport and electrical properties.

Synthetic geophysical EM data creation is based on the actual permeability model (Fig. 1a) and its corresponding hydrogeological flow state during CO_2 injection. In a first step, the function

$$\rho_f = \frac{\rho_{18C}}{1 + \alpha(T - 18)} \tag{1}$$

calculates pore fluid electrical resistivity ρ_f (with unit Ωm) from temperature T and content c of total dissolved solids (TDS), the latter affecting the reference resistivity at 18 degrees Celsius,

$$\rho_{18C} = \frac{3549}{c^{0.924}}. \tag{2}$$

Eq. (1) uses the constant $\alpha = 0.025$ which together with the constants in Eq. (2) reflects the temperature dependence of electrical resistivity as detailed by Hayashi (2004). These constants are chosen here as representative for the bulk resistivity ρ_b of the Sacramento River Delta region expressed by means of Archie's law,

$$\rho_b = a\phi^{-m}\rho_f, \tag{3}$$

where $a = 1$, ϕ is porosity, and the cementation exponent m varies between 1.1 for clay layers and 2 for sand layers. The bulk resistivity value of each model grid cell results from Eq. (3) and the cell's gas saturation value S_g,

$$\rho = \frac{1}{\sigma} = \frac{\rho_b}{(1-S_g)^n}, \tag{4}$$

using a constant exponent of $n = 2$. Our imaging method operates on the electrical conductivity $\sigma = \frac{1}{\rho}$ (with unit S/m). Eq. (4) represents the final petrophysical transformation function linking the (geophysical) σ-model to the reservoir flow model.

2.3. BSEM survey layout

Eqs. (1)-(4) represent the hydrogeophysical linkage between the modeling of the reservoir states of interest (between 8 and 12 years) and the corresponding geophysical property evolution. The outcome of Eq. (4) produces the model of electrical rock resistivity used to calculate synthetic data of a BSEM layout shown in Fig. 2. Recall that these data calculations are based on the ρ-distribution originating from the actual reservoir model. Synthetic data are given as electric fields that would be excited by borehole source antennas and measured via the surface electrode array. The employed controlled-source EM forward-modeling algorithm approximates Maxwell's equations on a finite-difference grid representing the geophysical modeling domain. Computational and algorithmic details can be found in the work of Commer and Newman (2008).

CSEM sources are deployed in monitoring wells U1 and U2 (indicated in Fig. 1 and Fig. 2). The sources are vertical electric dipole antennas with a length of 50 m, centered at a depth of 1850 m. We simulate data for both sources at four frequencies, 0.25, 0.5, 1, and 2 Hz. There are 13 north-south oriented receiver profiles spaced 250 m apart (along the Easting direction), with a receiver separation of 125 m (along the Northing direction). Two perpendicular electric-field components, E_x (parallel to Easting) and E_y (parallel to Northing) are recorded at 45 receiver stations per profile, thus amounting to a total of 585 stations and 1170 complex electric field data points per source frequency.

Magnitudes of artificial noise imposed on the synthetic data are based upon 0.5 % of the data amplitude and an additional noise floor of 10^{-12} V/m (normalized to unit dipole moment). Theoretical estimates for sensor noise-floor limits were reported between 10^{-14} V/m (Streich *et al.*, 2010) to 10^{-13} V/m (Wirianto *et al.*, 2010).

2.4. Simulating operational model uncertainty

Uncertainty in the understanding of reservoir processes is prevalent owing to monitoring data that is always insufficient in view of the reservoir system's size and complexity. Uncertainties associated with the history-matching process and the ensuing incompleteness of a given state-of-the-art reservoir model have been discussed at length (e.g., Subbey et al., 2004; Ma, 2011). Our scope touches on synthetic uncertainty, namely, does the ORM's incompleteness with respect to the actual model properly reflect the degree of incompleteness one would face in a corresponding real-world case?

Table 1 of Doughty and Oldenburg (2020) details reservoir properties of the actual model and the initial (at 0 years) ORM. Without going too much into detail, we reiterate here that the difference in permeability distribution, three-dimensionally heterogeneous versus layered (Fig. 1), already precludes the ORM from achieving a perfect data fit. Moreover, the ORM uses simpler relative permeability and capillary pressure functions. While both are based on the van Genuchten (1980) formulation, the actual model includes hysteresis and all function parameters depend on permeability. In contrast, the ORM is non-hysteretic and only the parameter capillary pressure strength depends on permeability via Leverett scaling.

The following initial reservoir conditions match their actuals by the 5-year stage of the ORM: Initial (hydrostatic) pressure, temperature (using a geothermal gradient), initial CH_4 (methane) distribution, and vertical salinity profile as derived from regional estimates by Kang and Jackson (2016). Note that CH_4 is initially absent and only becomes an added feature in the 5-year ORM. One could argue that a more realistic simulation of an incomplete ORM would involve more deviating initial conditions. However, assuming the existence of prior knowledge due to the site's depletion history, realistic deviations would not significantly affect the degree of error that is already present in the saturation predictions (Fig. 2). In other words, fine-scale improvements in the saturation prediction will not affect the geophysical plume imaging as the latter only requires a gross-scale saturation profile. More of these aspects are also discussed further below.

3. Constrained inversion of BSEM data

The total number of estimated parameters that make up the geophysical inversion domain amounts to 1,538,974 active finite-difference grid cells, where each cell hosts an electrical-conductivity parameter. The large discrepancy between the sizes of the parameter and data spaces causes solution ambiguity rendering the inverse problem ill-posed. Bound constraints aim at reducing the ambiguity by narrowing the solution space in zones where physical property ranges are known prior to inversion. The common approach reduces bound intervals according to the prior information's certainty (e.g., Kim and Kim, 2011). Our approach differs by widening bound intervals in zones where the ORM suggests significant time-lapse property changes. In the following, we describe the method of mapping the degree of gas saturation changes to its function parameters controlling spatially variable bound widths. The general concept of bound constraints was introduced earlier together with our employed inversion algorithm (Commer and Newman, 2008). The algorithm employs a non-linear conjugate gradient (NLCG) scheme which uses a line-search based upon quadratic interpolation, safeguarded with backtracking. Logarithmically transformed model parameters define the search space, which facilitates bound constraints as logarithmic functions are amenable to inequality constraints.

3.1. Spatially variable lower and upper parameter bounds for enhanced model resolution

Lower and upper parameter bounds are also known as inequality constraints (e.g., Kim et al., 1999) and are abbreviated by a and b in the following. Inequality refers to the evolution of a model parameter m during an inversion process, so that m is bounded by $a < m < b$. In order to impose a positivity constraint on electrical conductivity, the bounds usually occur in conjunction with logarithmic or hyperbolic types of parameter transformation functions. Generalized functions were formulated by Kim and Kim (2011),

$$x = \frac{1}{n}\log\left(\frac{m-a}{b-m}\right) = \frac{2}{n}\tanh^{-1}\left(\frac{2m-b-a}{b-a}\right); \qquad a < m < b, \tag{5}$$

where x is the transformed parameter and n is a positive integer constant. Our studies employ a version realized by $n = 1$. Other choices for n are discussed by Kim and Kim (2011). Transforming x back into the original model parameter space then leads to (Commer and Newman, 2008)

$$m = \frac{a + b\ \exp(x)}{1 + \exp(x)}; \qquad -\infty < x < \infty. \tag{6}$$

Constant bounds may be most suitable for inversion applications where no prior information is available, that is, the bound interval $[a, b]$ applies to every cell parameter m_i $(i = 1, \dots, M)$ of the finite-difference mesh representing the inversion domain. In the presence of location-dependent prior information, $[a, b]$ can become spatially variable so that each cell m_i is subjected to an individual bounding interval $[a_i, b_i]$.

3.2. Designing bounds from gas-saturation predictions

Gas saturation predictions provide the basis for constructing lower and upper conductivity parameter bounds in order to achieve a local resolution-enhancing effect. The general approach is to widen a preset default bound interval $[a, b] = [10^{-3}, 1.5]$ S/m within regions of interest, so that $[a, b]$ becomes $[a \cdot f_a, b \cdot f_b]$ with positive factors f_a and f_b. The choice of the default bounds are based on estimates of extremal conductivity values that result from reservoir modeling over the whole 12-year period of interest. The focus regions are linked to injection-induced gas saturation changes predicted from the ORM (Fig. 2b). With the focus being on delineating gas saturation changes between year 8 (quantified by S_g^{08y}) and year 12 (S_g^{12y}), the zones of interest are defined by their absolute percentage saturation change

$$\left|\Delta \mathrm{S}_g^{\%}\right| = \left|\frac{S_g^{12y} - S_g^{08y}}{S_g^{08y}}\right| \cdot 100 \tag{7}$$

exceeding a given threshold $\Delta \mathrm{S}_g^{thr\%}$. This threshold is set to $\Delta \mathrm{S}_g^{thr\%} = 5\ \%$ which is the minimum gas saturation change in percent that has to occur in order to augment the default interval $[a, b]$. In practice, the widening is achieved through two factors, $f_a = \frac{1}{f_{lb}(x,y,z)}$ and $f_b = f_{ub}(x, y, z)$, applied to $[a, b]$ so that the interval becomes spatially variable, $[a, b] \rightarrow \left[\frac{a}{f_{lb}}, b \cdot f_{ub}\right]$.

Dividing by the lower-bound factor $f_{lb} = f_{lb}\left(\Delta \mathrm{S}_g^{\%}\right)$ decreases the lower bound *a*. In our particular case, f_{lb} varies linearly between 1 and 100, i.e. $f_{lb}\left(\Delta \mathrm{S}_g^{\%} = 0\right) = 1$ and $f_{lb}\left(\Delta \mathrm{S}_g^{\%} \geq 100\right) = 100$. Hence, with higher saturation changes, the lower bound decreases up to a minimum of $^{a}/_{100}$. Enlarging the upper bound is achieved via multiplication of *b* with the factor f_{ub}, which varies linearly between 1 and 10, i.e. $f_{ub}\left(\Delta \mathrm{S}_g^{\%} = 0\right) = 1$ and $f_{ub}\left(\Delta \mathrm{S}_g^{\%} \geq 100\right) = 10$. The default bound interval thus increases to an extremum of $[a_{min}, b_{max}] = [10^{-5}, 15]$ S/m.

Setting the expansion factor for the lower bounds an order of magnitude larger than for the upper bounds reflects the fact that positive gas saturation changes and corresponding conductivity decreases dominate over the 12-year simulation period. Undocumented trial inversions with larger expansion factors, for example $f_{lb}\left(\Delta \mathrm{S}_g^{\%} \geq 100\right) = 1000$ and $f_{ub}\left(\Delta \mathrm{S}_g^{\%} \geq 100\right) = 100$, revealed no significant differences in the inversion outcome. Fig. 3 illustrates both bound extremes, the lower-bound (left) range $[a_{min}, a_{max}]$ and the upper-bound (right) range

$[b_{min}, b_{max}]$, for one vertical cross section. The selected plane is parallel to the Northing axes and cuts through the Easting coordinate at *E*=240 m.

Bounds construction starts by feeding the saturation S_g^{08y} and S_g^{12y}, calculated from the ORM, to Eq. (7). The output are sets of lower and upper bounds with augmented intervals for zones where the 5-%-threshold criterion is met. Upon input of the inversion's starting model, an individual bound pair a_i, b_i is then assigned to each cell parameter m_i of the inversion domain.

3.3. Gradient weighting and parameter masking

In addition to parameter bounds, we employ two other approaches that essentially impose constraints on the NLCG inversion process, namely gradient weighting and parameter masking. However, we abstain from a study that would systematically investigate the interplay of all three constraining methods as this would go beyond our intended scope. More systematic studies of combinations of different constraints were carried out by Portniaguine and Zhdanov (1999) and Boulanger and Chouteau (2001) in the context of gravity data inversion. Here, we use both gradient weighting and parameter masking in a rather empirical manner owing to their individually demonstrated benefit.

Gradient weighting as used in this work is a method of assigning weighting factors to each component of the gradient vector $\mathbf{g}$ of the NLCG scheme. The gradient vector $\mathbf{g}$ contains derivative information and is at the base of optimizing the direction of the line-search in model space. Methodological details and successful application of gradient weighting within the same NLCG scheme were demonstrated earlier (Commer et al., 2016). Principally, high sensitivities of cell parameters m_i pertaining to regions near surface spreads or instrumented wells are damped through assigning weighting factors $w_i < 1$. The corresponding weighted gradient component $w_i g_i$ then becomes down-weighted with respect to cells in unweighted model regions. Similar to the bound constraints, gradient weighting basically boosts the NLCG line-search in areas of low sensitivity, causing weak resolution, at the expense of high-sensitivity zones. For BSEM, the desired effect is to nudge model updates away from the vicinity of transmitters and receivers, where sensitivities are high, towards less resolved center regions.

Parameter masking as employed here is a straightforward way of disabling an arbitrary subset of cell parameters of a rectangular inversion domain. Geological horizons derived from seismic data usually provide the prior information needed to define parameter masks (e.g., Hoversten et al., 2021). We employ the upper horizon shown in Fig. 4 in order to deactivate all mesh cell parameters that are above it. The underlying assumption is a no-leakage scenario, that is, our imaging objective does not consider the case of buoyancy-driven gas flow into the caprock. The present inversion study assumes that the background geology above the delineating seismic horizon would be known from preliminary baseline (pre-injection) data inversions and prior information.

3.3. Sequential inversion scheme

Delineating property changes between the two observation times (8 years and 12 years after the start of injection) involves a three-step inversion procedure. Three inversion runs pertain to the refinement of the baseline (pre-injection) model and, with respect to this baseline, the delineation of fluid-induced anomalous resistivity alterations after 8 and 12 years. Synthetic time-lapse data for these inversions are obtained by using the actual reservoir model and the BSEM configuration for three times, referred to as Year00, Year08, and Year12. For these times, Eqs. (1)-(4) convert the corresponding flow properties (porosity, saturation, and content of TDS) to electrical conductivity (σ).

The first step of the inversion sequence refines the 3D baseline model. Fig. 4 shows slices along the Northing direction for the initial σ-distribution resulting from the transform of the pre-injection state calculated for the actual (left) and ORM (right). The latter one is the starting model for the first NLCG inversion sweep which refines the pre-injection state (at year 0) below the upper seismic horizon (annotated in Fig. 4, cell parameters are fixed above). The output $\sigma(\text{Year00})$ serves as the starting model for the second inversion sweep, estimating the σ-distribution after 8 years of injection. In the third sweep, the estimated model $\sigma(\text{Year08})$ then becomes the initial guess for the delineation of the plume after 12 years of injection, the output referred to as $\sigma(\text{Year12})$.

We perform the three-step inversion sequence twice in a comparative way. The first sequence uses constant lower and upper parameter bounds $[a, b] = [10^{-5}, 15]$ S/m; the second uses variable bounds (Fig. 3), $[a, b] = \left[\frac{a}{f_{lb}}, b \cdot f_{ub}\right]$, that widen according to the factors f_{lb} and f_{ub} as described above. Variable bounds are active only for the estimation of the Year08 and Year12 states, that is, both inversion sequences employ constant bounds for the Year00-inversion. Note that the constant-bound sequence uses the extremal interval $[a_{min}, b_{max}]$ occurring in the variable-bound inversion sequence. The initial reasoning for a globally wide interval was to let the inversion practically be unbounded in order to avoid any bias due to potentially too tight bounds. However, other undocumented trial inversion experiments with the narrower default bound interval $[a, b] = [10^{-3}, 1.5]$ S/m yielded no significant difference in the final model outcomes.

Computing times amounted to a total of 126 hours for the inversion sequence with constant bounds versus 147 total hours for the variable-bounds sequence. All inversions employed 250 cores of a cluster architecture with Intel Cascade Lake processor compute nodes (40 cores per node) connected with a Mellanox EDR infiniband fabric.

4. Results and Discussion

The final plume image output is represented in Fig. 5 as differences in σ between the estimated Year08 and Year12 models. We compare the differences $\Delta\sigma = \sigma(\text{Year12}) - \sigma(\text{Year08})$ in percent for two realizations of the three-step sequential inversion outlined above. The first uses constant bounds, the second uses spatially variable bounds. Fig. 5a shows the true distribution $\Delta\sigma^{true}$ which is calculated from the petrophysical transform of the actual reservoir model state at Year08 and Year12. Fig. 5b and Fig. 5c compare the estimated counterparts, these are, respectively, the differences $\Delta\sigma^{con}$ (constant bounds) and $\Delta\sigma^{var}$ (variable bounds). Negative changes greatly dominate in the actual outcome $\Delta\sigma^{true}$ and are visualized here since our inversion objective focuses on the time-lapse accumulation of CO_2 which causes negative time-lapse changes.

Most notable between the two estimates $\Delta\sigma^{con}$ and $\Delta\sigma^{var}$ is a lack of delineation of any property changes in zones of interest away from the injection well for the image $\Delta\sigma^{con}$. In contrast, $\Delta\sigma^{var}$ exhibits the fluid-induced property alterations across the regional scale. The variable-bound method thus yields indicators for negative time-lapse changes associated with CO_2 accumulation and migration. Deviations from the true case manifest in an overestimated volume undergoing fluid-induced conductivity alterations in the Northern attic region. Concurrently, conductivity decreases in the region around the wells U1 and U2 remain underestimated in terms of their magnitudes.

A certain degree of image blurring can be expected from CSEM inversions of low-frequency data, because model resolution is limited due to corresponding large wavelengths of the generated EM fields. However, despite the low resolution and the limited coverage using two transmitter wells, the final image of $\Delta\sigma^{var}$ is sufficient to support predictions of CO_2-breakthrough in the Northern attic region (Fig. 2b) with first-order accuracy. For this zone, Fig. 2 revealed a discrepancy in the elevation of predicted saturation changes (between Year08 and Year12). This discrepancy appears only marginally in the image $\Delta\sigma^{var}$.

The large image improvement provided by the modified bounds indicates an optimization of the model-updating line-search procedure. In essence, the method translates to steering and scaling the conjugate search direction of our NLCG inversion scheme such that it more closely resembles the Newton direction. The latter is characterized by faster convergence and less potential for a premature end of the line-search in a local minimum, yet is computationally very expensive. This point of view also hints at a resemblance with the method of regularized focusing inversion (Portniaguine and Zhdanov, 1999), where stabilizing functionals convey prior information with the goal of image focusing.

5. Conclusions

Spatially variable lower and upper parameter bounds provide a straightforward way of incorporating prior model information in an inversion workflow. Our example inversion studies demonstrated that such prior model information can be obtained through rough spatial estimates of anticipated fluid-induced property alterations. Regions of property alterations that qualify as anomalous with respect to the property range of the underlying baseline geology are target zones of interest in time-lapse imaging problems. Prior-model information of such target zones translates to enlarged bound intervals. Our inversion study demonstrated that widened bound intervals can selectively enhance model resolution in target zones. Spatially balanced bounds can thus greatly improve the imaging process through their potential of steering the NLCG search direction away from local solution minima.

Since reservoir modeling will likely be a minimum required tool for GCS site management, it represents an inexpensive source of auxiliary information for constraining geophysical plume imaging problems. One may thus call the presented method a "poor people's approach" to hydrogeophysical data analysis, because inexpensive also holds for the relative simplicity in incorporating flow information as parameter bounds. Approximate bound intervals make the method somewhat forgiving towards petrophysical uncertainties while still constraining geophysical parameter estimation to the physical processes of the flow system. In contrast, more rigorous and involved fully-coupled hydrogeophysical joint inversion approaches are generally susceptible towards erroneous petrophysical relationships (e.g., Sun and Li, 2017).

In light of a need for cost-effective monitoring, our synthetic experiments consider limitations likely present at future GCS sites. A relatively sparse volume coverage results from employing two existing monitoring wells for source deployment. However, fluid-induced conductivity alterations could still be mapped, suggesting that the variable-bounds concept can help offset model resolution loss due to limited survey coverage.

While we deem the simulated BSEM survey layout as relatively economic, more involved studies similar to the works of Eidsvik et al. (2008) and Trainor-Guitton et al. (2014) could figure out an informative cost measure in form of a benefit-cost ratio. Such a measure would essentially help the operator decide whether the BSEM data's added value in form of more accurate plume predictions outweighs the survey costs. Eidsvik et al. (2008) used the decision-theoretic concept of value of information (VOI) with rock physics and spatial statistics in order to compare the value of seismic amplitude-versus-offset data against CSEM. In our case, this comparison would be between well-based reservoir monitoring data against BSEM data.

Trainor-Guitton et al. (2014) presented a VOI methodology that quantifies the impact of inaccuracies of multidimensional geophysical inversions on geothermal resource identification. Translated to GCS contexts, a VOI assessment of constrained EM data inversions as presented here might help analyze aspects of interest to the operator that go beyond cost, for example leakage risk and environmental impact.

A final related comment concerns ORM uncertainty, as discussed in Section 2.4., as a major factor influencing VOI of BSEM monitoring. Despite fairly significant deviations from the actual model, the 5-year ORM produced a gross-scale match of the actual gas saturation that turned out sufficient for the bound construction and ensuing delineation of anticipated target zones. A follow-up study similar to Harp et al. (2019) would investigate at what point larger deviations, caused by larger ORM parameter errors, would render the BSEM imaging outcome too distorted. Harp et al. (2019) developed a metric for quantifying the degree to which ORM parameters can deviate from their actuals without violating preset reservoir performance criteria. We envision a similar kind of robustness measure for assessing when an ORM may become too erroneous for properly constraining geophysical reservoir imaging.

ACKNOWLEDGMENTS

Support for this project comes from the U.S. Department of Energy (DOE) Office of Fossil Energy's Crosscutting Research Program. Work was completed under the U.S. DOE Contract No. DE-AC02-05CH1123 as part of the National Risk Assessment Partnership (NRAP) project.

REFERENCES

Abubakar, A, Habashy, T.M., Druskin, V.L., Knizhnerman, L., Alumbaugh, D., 2008. 2.5D forward and inverse modeling for interpreting low-frequency electromagnetic measurements. Geophysics 73, F165-F177.

Aghamiry, H.S., Gholami, A., Operto, S., 2019. Implementing bound constraints and total-variation regularization in extended full waveform inversion with the alternating direction method of multiplier: Application to large contrast media. Geophys. J. Int. 218, 855-872.

Alemu, B.L., Aker, E., Soldal, M., Johnsen, Ø., Aagaard, P., 2011. Influence of CO_2 on rock physics properties in typical reservoir rock: A CO_2 flooding experiment of brine saturated sandstone in a CT-scanner. Energy Procedia 4, 4379-4386.

Arts, R.J., Chadwick, A., Eiken, O., Thibeau, S., Nooner, S., 2008. Ten years' experience of monitoring CO_2 injection in the Utsira Sand at Sleipner, offshore Norway. First break, 26 (1), 65-72.

Ayani, M., Dario, G., Liu, M., 2020. Stochastic inversion method of time-lapse controlled source electromagnetic data for CO2 plume monitoring. Int. J. Greenh. Gas Control 100, 103098.

Boulanger, O., Chouteau, M., 2001. Constraints in 3D gravity inversion. Geophysical Prospecting 49, 265-280.

Commer, M., Newman, G.A., 2008. New advances in three-dimensional controlled-source electromagnetic inversion, Geophys. J. Int. 172, 513-535.

Commer, M., Doetsch J., Dafflon B., Wu Y., Daley T.M., Hubbard S.S., 2016. Time-lapse 3-D electrical resistance tomography inversion for crosswell monitoring of dissolved and supercritical CO2 flow at two field sites: Escatawpa and Cranfield, Mississippi, USA. Int. J. Greenh. Gas Control, 49, 297-311.

Commer, M., Alumbaugh, D.A., Hoversten, G.M., Um, E.S., Vasco, D.W., Wilt, M., Nichols, E., Marchesini, P., Macquet, M., 2022. Enhanced multi-dimensional inversion through target-specific inversion parameter bounds with an application to crosswell EM for sequestration monitoring, submitted to Frontiers in Earth Science.

Davis, T.L., Landrø, M., Wilson, M., 2019. Geophysics and geosequestration. Cambridge University Press.

Doughty, C., Oldenburg, C.M., 2020. CO_2 plume evolution in a depleted natural gas reservoir: Modeling of conformance uncertainty reduction over time. Int. J. Greenh. Gas Control 97, 103026.

Eidsvik, J., Bhattacharjya, D., Mukerji, T., 2008. Value of information of seismic amplitude and CSEM resistivity. Geophysics 73. R59-R69.

Gasperikova, E., Hoversten, G.M., 2006. A feasibility study of non-seismic geophysical methods for monitoring geologic CO_2 sequestration. The Leading Edge, 25 (10), 1282–1288.

Gasperikova, E., Appriou, D., Bonneville, A., Feng, Z., Huang, L., Gao, K., Yang, X., Daley, T., 2022. Sensitivity of geophysical techniques for monitoring secondary CO_2 storage plumes, Int. J. Greenh. Gas Control 114, 103585.

Grana, D., Liu, M., Ayani, M., 2021. Prediction of CO_2 saturation spatial distribution using geostatistical inversion of time-lapse geophysical Data. IEEE Trans. Geosci. Rem. Sens. 59, 3846-3856.

Grayver, A.V., Streich, R., Ritter, O., 2014. 3D inversion and resolution analysis of land-based CSEM data from the Ketzin CO2 storage formation. Geophysics 79 (2), E101-E114.

Girard, J.-F., Coppo, N., Rohmer, J., Bourgeois, B., Naudet, V., Schmidt-Hattenberger, C., 2011. Time-lapse CSEM monitoring of the Ketzin (Germany) CO_2 injection using 2xMAM configuration. Energy Procedia 4, 3322-3329.

Harp, D.R., Oldenburg, C.M., Pawar, R., 2019. A metric for evaluating conformance robustness during geologic CO_2 sequestration operations. Int. J. Greenh. Gas Control. 85, 100-108.

Hayashi, M., 2004. Temperature-electrical conductivity relation of water for environmental monitoring and geophysical data inversion. Environmental monitoring and assessment 96. 119 -128.

He, Z., Liu, X., Qiu, W., Huang, Z., 2005. Mapping reservoir boundary by borehole-surface TFEM: two case studies. Lead. Edge, 24 (9), 898-900.

Hosseini, S.A., Lashgari, H., Choi, J.W., Nicot, J.-P., Lu, J., Hovorka, S.D., 2013. Static and dynamic reservoir modeling for geological CO_2 sequestration at Cranfield, Mississippi, U.S.A. Int. J. Greenh. Gas. Contr. 18, 449-462.

Hoversten, G.M., Mackie, R.L., Hua, Y., 2021. Reexamination of controlled-source electromagnetic inversion at the Lona prospect, Orphan Basin Canada. Geophysics 86 (3), E157–E170.

Jenkins, C., Chadwick, A., Hovorka, S.D., 2015. The state of the art in monitoring and verification - ten years on. Int. J. Greenh. Gas Contr., 40, 312–349.

Kang, M., Jackson, R.B., 2016. Salinity of deep groundwater in California: Water quantity, quality, and protection. Proc. Nat. Acad. Sci. 113 (28), 7768-7773.

Kim, H.J., Song, Y., Lee, K.H., 1999. Inequality constraint in least-squares inversion of geophysical data. Earth Planets Space 51, 255-259.

Kim, J., Xue, Z., Matsuoka, T., 2010. Experimental study of CO_2 monitoring and saturation with combined P-wave velocity and resistivity, CPS/SPE Int. Oil & Gas Conf. and Exhib., SPE 130284.

Kim, H.J., Kim Y.H., 2011. A unified transformation function for lower and upper bounding constraints on model parameters in electrical and electromagnetic inversion, Journal of Geophysics and Engineering 8, 21–26.

Ma, Y.Z., 2011. Uncertainty analysis in reservoir characterization and management: How much should we know about what we don't know?, in: Ma, Y.Z., La Pointe, P.R. (Eds.), Uncertainty analysis and reservoir modeling. AAPG Memoir 96, pp. 1–15.

Marsala, A.F., Al-Buali, M.H., Ali, Z.A., Ma, S.M., He, Z., Biyan, T., Zhao, G., He, T., 2011. First pilot of borehole to surface electromagnetic in Saudi Arabia: A new technology to enhance reservoir mapping and monitoring, 73rd Annual Int. Conf. and Exhibition, EAGE, Extended Abstracts, I005.

Marsala, A.F., Zhdanov, M.S, Endo, M., Black, N., 2014. 3D inversion of borehole to surface electromagnetic data in a multiple reservoirs survey, 84th Annual Int. Meeting, SEG, Denver, USA, Expanded Abstracts, 2600-2604.

Michael, K., Golab, A., Shulakova, V., Ennis-King, J., Allinson, G., Sharma, S., and Aiken, T., 2010. Geological storage of CO_2 in saline aquifers - A review of the experience from existing storage operations. Int. J. Greenhouse Gas Control, 4, 659-667.

Ogarko, V., Giraud, J., Martin, R., and Jessell, M., 2021. Disjoint interval bound constraints using the alternating direction method of multipliers for geologically constrained inversion: Application to gravity data. Geophysics 86, G1-G11.

Oldenburg, C.M., Pruess, K., Benson, S.M., 2001. Process modeling of CO2 injection into natural gas reservoirs for carbon sequestration and enhanced gas recovery. Energy and Fuels 15, 293-298.

Portniaguine, O., Zhdanov, M.S., 1999. Focusing geophysical inversion images. Geophysics 64 (3), 874-887.

Ringrose, P., 2020. How to store CO_2 underground: insights from early-mover CCS projects, Springer, Berlin/Heidelberg.

Schaller, A., Hunziker, J., Streich, R., Drijkoningen, G., 2014. Sensitivity of the near-surface vertical electric field in land controlled- source electromagnetic monitoring, 84th Annual Int. Meeting, SEG, Denver, USA, Expanded Abstracts, 838–843.

Shi, J.-Q., Durucan, S., Fujioka, M., 2008. A reservoir simulation study of CO_2 injection and N_2 flooding at the Ishikari coalfield CO_2 storage pilot project, Japan. Int. J. Greenh. Gas Control, 2 (1), 47-57.

Sosa, A., Velasco, A.A., Velazquez, L., Argaez, M., and Romero, R., 2013. Constrained optimization framework for joint inversion of geophysical data sets. Geophys. J. Int. 195, 1745-1762.

Streich, R., Becken, M., Ritter, O., 2010. Imaging of CO_2 storage sites, geothermal reservoirs, and gas shales using controlled-source magnetotellurics: Modeling studies. Chemie der Erde 70 (S3), 63–75.

Subbeya, S., Christie, M., Sambridge, M., 2004. Prediction under uncertainty in reservoir modeling. J. Petrol. Sci. Eng. 44 (1-2), 143-153.

Sun, J., Li, Y., 2017. Joint inversion of multiple geophysical and petrophysical data using generalized fuzzy clustering algorithms. Geophys. J. Int. 208, 1201-1216.

Trainor-Guitton, W., Hoversten, G.M., Ramirez, A., Roberts, J., Juliusson, E., Key, K., Mellors, R., 2014. The value of spatial information for determining well placement: A geothermal example. Geophysics 79 (5), W27-W41.

Tveit, S., Bakr, S.A., Lien, M., Mannseth, T., 2015. Ensemble-based Bayesian inversion of CSEM data for subsurface structure identification. Geophys. J. Int., 201 (3), 1849-1867.

Tveit, S., Mannseth, T., Park, J., Sauvin, G., Agersborg, R., 2020. Combining CSEM or gravity inversion with seismic AVO inversion, with application to monitoring of large-scale CO2 injection. Computational Geosciences 24, 1201-1220.

Tveit, S., Mannseth, T., 2022. Monitoring of large-scale CO2 injection using CSEM, gravimetric, and seismic AVO data, in: Huang, L. (Ed.), Geophysical Monitoring for Geologic Carbon Storage. American Geophysical Union, pp. 273-301.

Van der Meer, L.G.H., 1993. The conditions limiting CO_2 storage in aquifers. Energy Conversion and Management 34 (9), 959-966.

van Genuchten, M.Th., 1980. A closed-form equation for predicting the hydraulic conductivity of unsaturated soils. Soil Sci. Soc. Am. J. 44 (5), 892–898.

Vilamajó, E., Queralt, P., Ledo, J., Marcuello, A., 2013. Feasibility of monitoring the Hontomín (Burgos, Spain) CO2 storage site using a deep EM source. Surveys in Geophysics 34, 441–461.

Wirianto, M., Mulder, W.A., Slob, E.C., 2010. A feasibility study of land CSEM reservoir monitoring in a complex 3-D model. Geophysical Journal International 181, 741–755.

Yi, M.-J., Kim, J.H., Chung, S.-H., 2003. Enhancing the resolving power of least-squares inversion with active constraint balancing. Geophysics 68, 931–941.

Figures

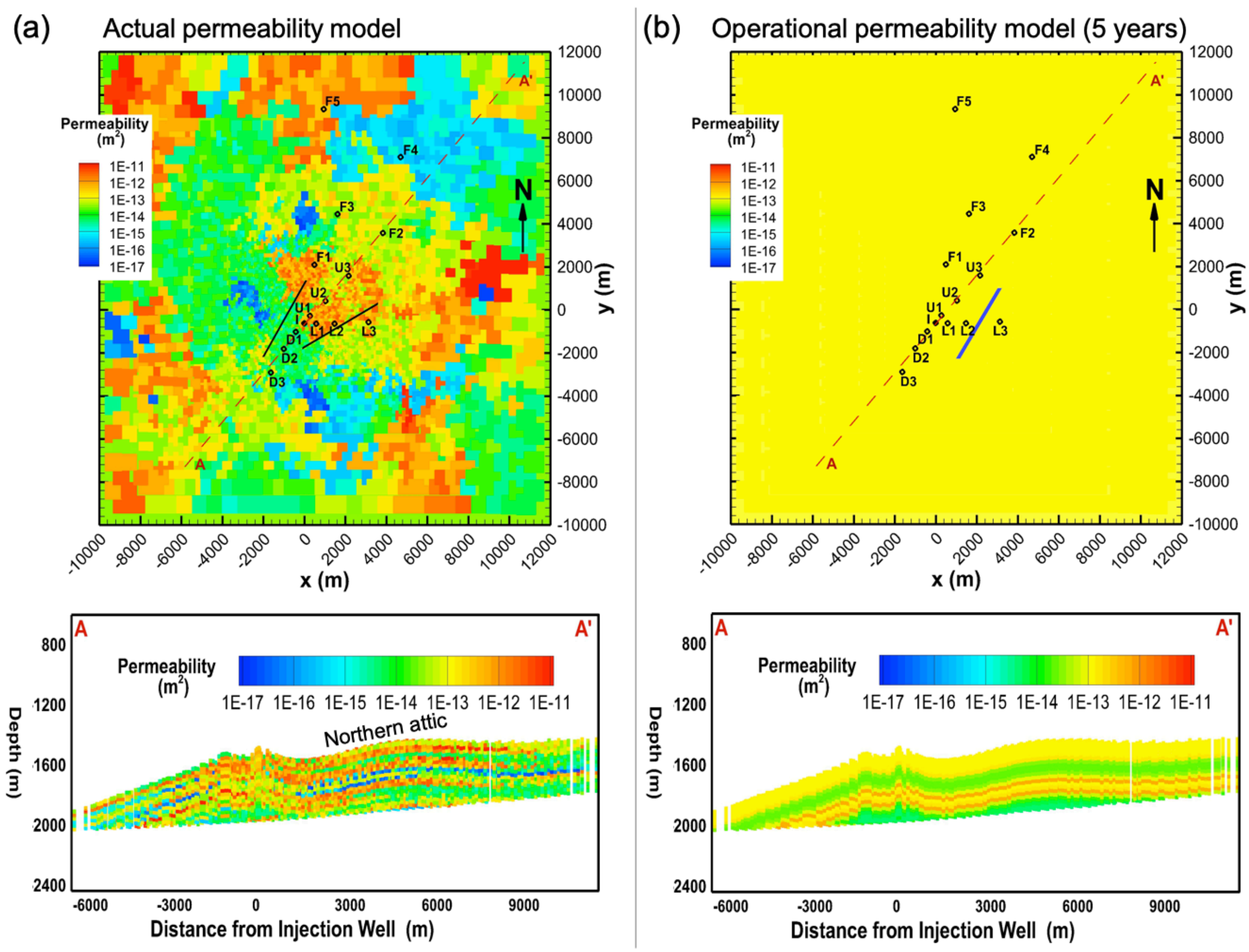

Fig. 1: Actual (a) and operational (b) permeability model. Vertical slices (lower subplots) are along the diagonal (A-A', dashed) line and show the stratified reservoir heterogeneity with high-permeability attic zones. The actual model features vertical faults as black line segments (one blue line in the simplified model). Vertical exaggeration is two times. Note that the (x-y) plan views are not horizontal as they are a projection of the top layer in the reservoir model.

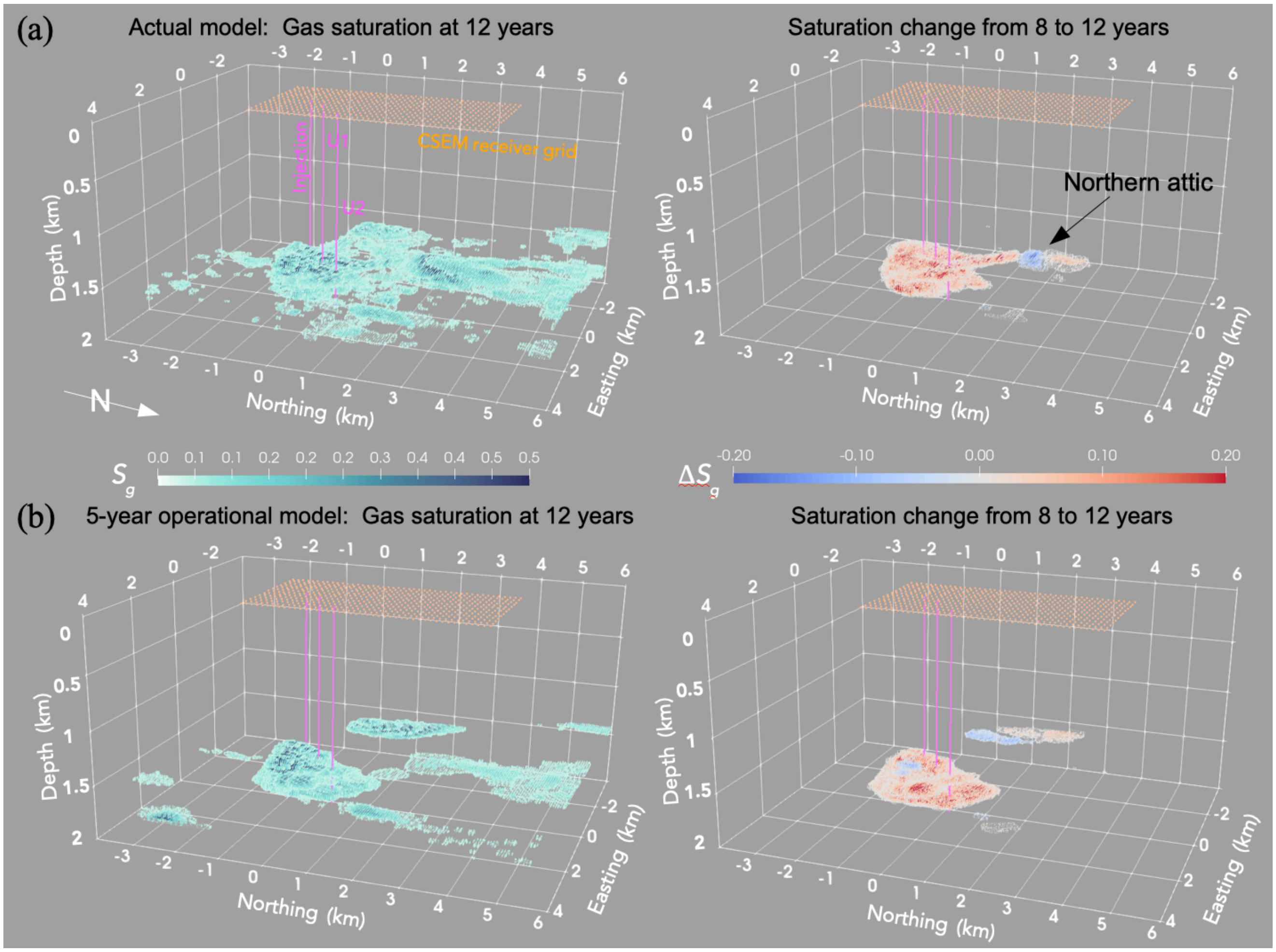

Fig. 2: Gas saturation predictions calculated from the actual (a) and 5-year operational (b) reservoir flow model. The right plot column shows gas saturation differences between predictions made at 8 and 12 years. Each monitoring well U1 and U2 hosts one borehole EM transmitter at a depth of 1850 m, sourcing the shown surface receiver grid. Receiver profiles extend from y=-1500 m to y=4000 m, with a station interval of Δy=125 m.

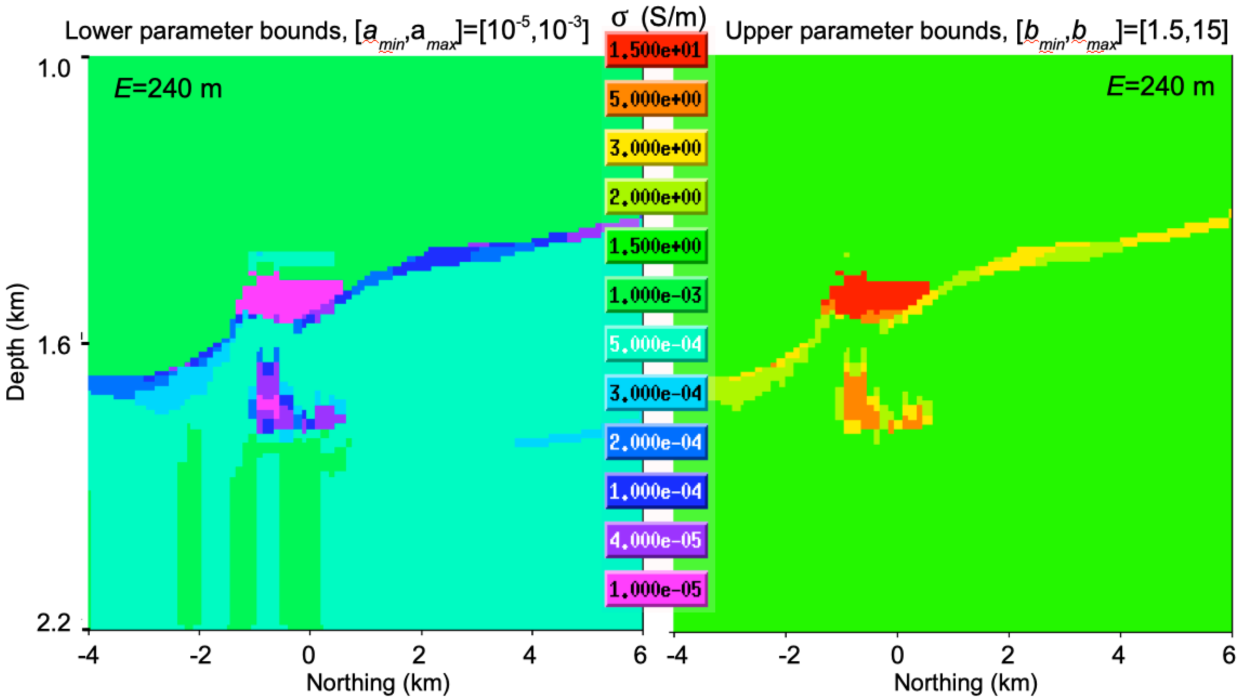

Fig. 3: Augmented lower and upper parameter bounds. The example cross sections are through the Easting coordinate *E*=240 m.

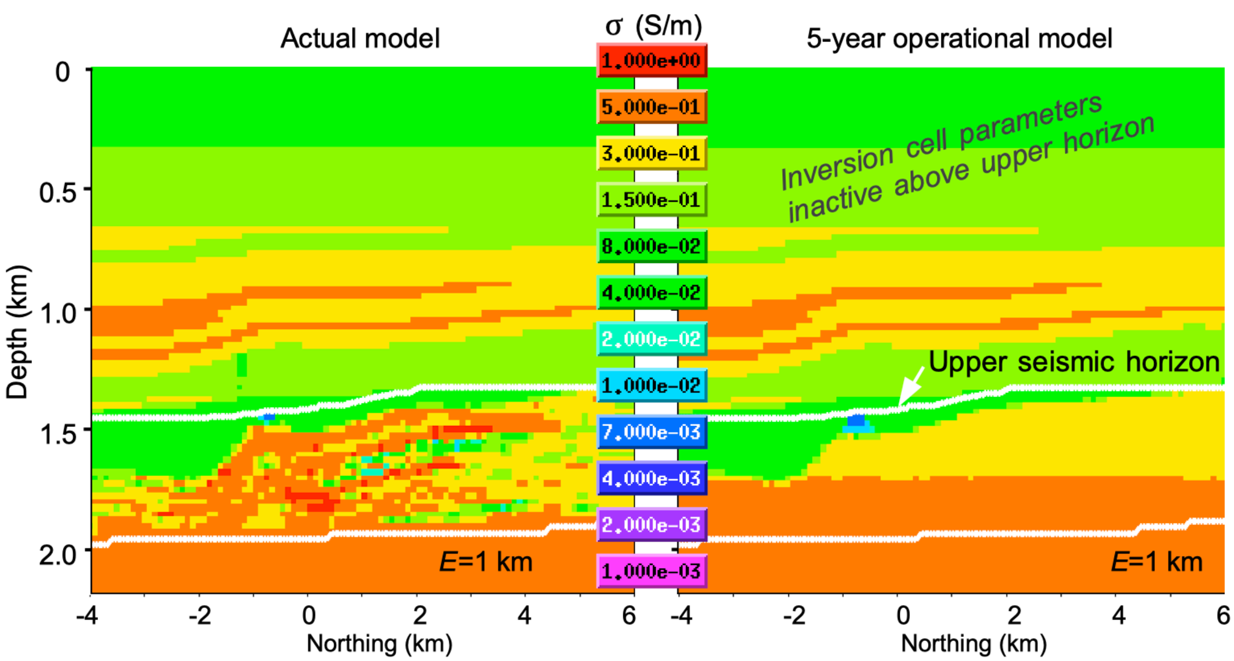

Fig. 4: Petrophysical transform of the actual (left) and operational (right) flow model into the baseline (Year00) electrical conductivity. Conductivities derived from the operational model serve as the initial model guess for the inversion that refines the Year00 (pre-injection) model

below the upper seismic horizon (indicated by the white lines). The upper horizon delineates the upper boundary of the inversion domain.

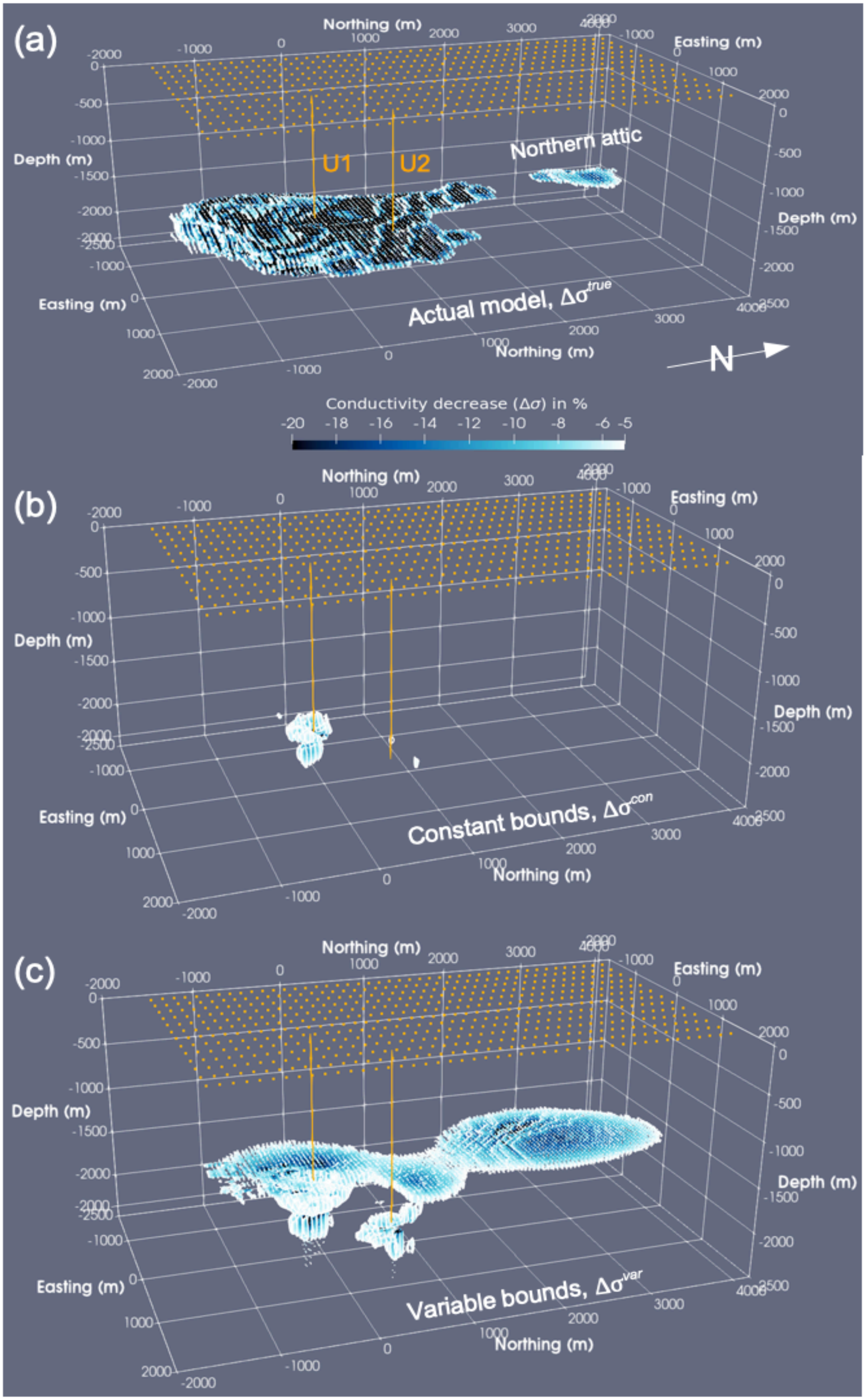

(a)
Northing (m)
Easting (m)
Depth (m)
U1
U2
Northern attic
Actual model, $\Delta\sigma^{true}$
N
Conductivity decrease ($\Delta\sigma$) in %
(b)
Constant bounds, $\Delta\sigma^{con}$
(c)
Variable bounds, $\Delta\sigma^{var}$

Fig. 5: Electrical conductivity change $\Delta\sigma = \sigma(\text{Year12}) - \sigma(\text{Year08})$ resulting from the corresponding gas saturation changes between Year08 and Year12. (a) True difference $\Delta\sigma^{true}$ calculated from the actual model. (b) Estimated difference $\Delta\sigma^{con}$ resulting from the constant-bound inversion sequence. (c) Estimated difference $\Delta\sigma^{var}$ resulting from the variable-bound inversion sequence.